Raman spectroscopy and x-ray diffraction of sp^3 CaCO$_3$ at lower mantle pressures

Sergey S. Lobanov,[1,2,*] Xiao Dong,[3] Naira S. Martirosyan,[1,2] Artem I. Samtsevich,[4] Vladan Stevanovic,[5]
Pavel N. Gavryushkin,[2,6] Konstantin D. Litasov,[2,6] Eran Greenberg,[7] Vitali B. Prakapenka,[7]
Artem R. Oganov,[4,8,9,10] and Alexander F. Goncharov[1,11]

[1]*Geophysical Laboratory, Carnegie Institution of Washington, Washington, D.C. 20015, USA*

[2]*Sobolev Institute of Geology and Mineralogy, Siberian Branch, Russian Academy of Sciences, 3 Prospekt Akademika Koptyuga, Novosibirsk 630090, Russia*

[3]*Center for High Pressure Science and Technology Advanced Research, Beijing 100193, China*

[4]*Skolkovo Institute of Science and Technology, Skolkovo Innovation Center, 5 Nobel Street, Moscow 143026, Russia*

[5]*Department of Metallurgical and Materials Engineering, Colorado School of Mines, Golden, Colorado 80401, USA*

[6]*Laboratory of Experimental Geochemistry and Petrology of the Earth's Mantle, Novosibirsk State University, Novosibirsk 630090, Russia*

[7]*Center for Advanced Radiation Sources, University of Chicago, Chicago, Illinois 60632, USA*

[8]*Moscow Institute of Physics and Technology, 9 Institutskiy Lane, Dolgoprudny City, Moscow Region 141700, Russia*

[9]*School of Materials Science, Northwestern Polytechnical University, Xi'an 710072, China*

[10]*Department of Geosciences, Center for Materials by Design, Institute for Advanced Computational Science, Stony Brook University, Stony Brook, New York 11794, United States*

[11]*Key Laboratory of Materials Physics, Institute of Solid State Physics, CAS, Hefei 230031, China*

The exceptional ability of carbon to form sp^2 and sp^3 bonding states leads to a great structural and chemical diversity of carbon-bearing phases at nonambient conditions. Here we use laser-heated diamond-anvil cells combined with synchrotron x-ray diffraction, Raman spectroscopy, and first-principles calculations to explore phase transitions in CaCO$_3$ at $P > 40$ GPa. We find that postaragonite CaCO$_3$ transforms to the previously predicted $P2_1/c$ CaCO$_3$ with sp^3-hybridized carbon at 105 GPa ($\sim$30 GPa higher than the theoretically predicted crossover pressure). The lowest-enthalpy transition path to $P2_1/c$ CaCO$_3$ includes reoccurring sp^2 and sp^3 CaCO$_3$ intermediate phases and transition states, as revealed by our variable-cell nudged-elastic-band simulation. Raman spectra of $P2_1/c$ CaCO$_3$ show an intense band at 1025 cm^{-1}, which we assign to the symmetric C-O stretching vibration based on empirical and first-principles calculations. This Raman band has a frequency that is $\sim$20% lower than the symmetric C-O stretching in sp^2 CaCO$_3$ due to the C-O bond length increase across the sp^2-sp^3 transition and can be used as a fingerprint of tetrahedrally coordinated carbon in other carbonates.

I. INTRODUCTION

The thermodynamic ground state of carbon at ambient conditions is graphite with a triangular bonding pattern (sp^2 hybridization). High pressure P, however, favors tetrahedrally bonded (sp^3) carbon, and diamond is stable at $P > 1.7$ GPa (0 K) [1]. The different bonding patterns of graphite and diamond result in very different mechanical, optical, electric, and thermal properties [2], making carbon a truly remarkable element. On top of this, carbon forms very strong directional bonds, leading to high melting temperatures T as well as high activation energies for the solid-state phase transitions [1]. As a result, carbon has a rich variety of metastable phases with mixed sp^2 and sp^3 bonding patterns that may integrate the unique physical properties of both graphite and diamond [3,4]. The synthesis of such novel carbon-based technological materials requires navigating in the carbon energy landscape as well as insights into the trajectories and mechanisms of its phase transitions [5].

Unlike carbon, the thermodynamically stable form of silicon at ambient conditions has the cubic diamond structure. Not surprisingly, nearly all low-pressure silicates incorporate silicon exclusively in the form of sp^3-hybridized SiO$_4$

tetrahedral groups. The electronic structure of SiO$_4$ tetrahedra is such that each oxygen has a half-occupied p orbital available for polymerization with adjacent groups. The topology of polymerized SiO$_4$ networks largely governs the physical properties of silicates and serves as the basis for their structural classification [6,7]. On the other hand, sp^2-hybridized CO$_3$ triangular groups have an additional C-O π bond and, as a result, are isolated in the crystal structures of carbonates. This difference in the electronic structures of CO$_3$ and SiO$_4$ groups leads to very different physical properties of sp^2 carbonates and sp^3 silicates. At high pressure, however, the electronic structure of carbon in carbonates may change via the C-O π-bond polymerization as individual CO$_3$ groups approach each other. Theoretical computations predict that sp^3 carbonates become thermodynamically stable at $P > \sim$ 80–130 GPa [8–12]. Here we investigate the high-P behavior of CaCO$_3$, one of the most abundant carbonates near the Earth's surface and a good proxy for carbonate chemical composition in the mantle [13,14].

Previous high-P studies have revealed a number of pressure-induced transformations in CaCO$_3$. At $P < \sim$40 GPa, (meta)stable phases of CaCO$_3$ include calcite, aragonite, CaCO$_3$ II, CaCO$_3$ III, CaCO$_3$ IIIB, and CaCO$_3$ VI (e.g., [9,15–17]). At $P > 40$ GPa, CaCO$_3$ transforms into postaragonite, which has been reported as a stable phase up to 137 GPa [9,18,19]. Importantly, all these structures contain sp^2-hybridized carbon forming triangular CO$_3$ groups.

*slobanov@carnegiescience.edu; slobanov@igm.nsc.ru

Pyroxene-like $C222_1$ $CaCO_3$, which has been predicted to be stable at $P > 137$ GPa, has a different bonding pattern, with sp^3-hybridized carbon forming polymerized CO_4 chains [9]. This prediction gained some experimental support in that the major Bragg peaks of the $C222_1$ $CaCO_3$ were observed in experiment at $P > 140$ GPa [19]. The high synthesis pressure implied that sp^3 $CaCO_3$ is not present in the Earth's mantle (135 GPa is the core-mantle boundary pressure), and further experimental studies of sp^3 carbonates were shifted to other compositions. More recently, the sp^2-sp^3 transition in $CaCO_3$ was revisited by Pickard and Needs [12], who predicted a new sp^3 $CaCO_3$ phase ($P2_1/c$) at $P > 76$ GPa, calling for a new synthesis study.

Here we explore phase transitions in $CaCO_3$ at $P > 40$ GPa via synchrotron x-ray diffraction, Raman spectroscopy, and first-principles calculations. We establish the stability field of sp^3-bonded $P2_1/c$ $CaCO_3$ and show that this phase has a strong Raman band characteristic of fourfold carbon in its crystal structure. We provide computational insights into the sp^2-sp^3 phase-transition mechanism, which in $CaCO_3$ appears to be a complex multistage process. Finally, our results support the notion of the effect of sp^2-sp^3 crossover on the carbonate crystal chemistry in the lower mantle.

II. METHODS

A. Experimental methods

Diamond-anvil cells (DACs) equipped with flat 200–300-μm culets were used to generate high pressure. Rhenium gaskets ($\sim$200 μm thick) were indented to $\sim$30–40 μm by the anvils and laser drilled in the center of the indentation in order to prepare a sample chamber with a diameter of 70–120 μm. The sample chamber was loaded with 99.95% $CaCO_3$ (Alfa Aesar) mixed with Pt powder (20%–30%), which served both as a heating laser absorber and as a pressure standard [20]. No pressure-transmitting medium was used in the experiments.

X-ray diffraction (XRD) measurements and laser heatings were performed at the 13ID-D GeoSoilEnviroCARS beamline (Argonne National Lab, Advanced Photon Source) that allows *in situ* XRD collections at extreme P-T conditions and a subsequent high-resolution mapping of the sample quenched to ambient temperature [21]. At all pressures a typical heating cycle involved (i) stepwise heating up to $T \sim 2000$ K, while following the diffraction pattern each 100–200 K; (ii) annealing at $T \sim 2000$ K, at which temperature we typically observed the formation of new XRD peaks, while moving the samples by $\sim$10 μm in horizontal and vertical directions (1-μm step); and (iii) quenching and mapping the heated region in order to find areas with less Pt and more $CaCO_3$. The x-ray energy was 37–42 keV focused to an $\sim$3 $\times$ 4 μm spot. Two-dimensional XRD images were integrated using the DIOPTAS software [22] for online analyses. Selected XRD patterns were analyzed in POWDERCELL 2.4 and Le Bail refined in GSAS/EXPGUI [23,24]. Equation-of-state fitting was performed using EOSFIT7GUI [25] and VESTA [26] was used for structure visualization.

After the synthesis and XRD measurements, samples with sp^3 $CaCO_3$ were characterized by Raman spectroscopy upon decompression at the Geophysical Laboratory using solid-state

488-nm (Spectra-Physics), 532-nm (Laser Quantum GEM), and 660-nm (Laser Quantum Ignis) laser excitations focused to a 3–4-μm spot size in diameter. The use of three excitation wavelengths allows unambiguously identifying bands that are Raman in origin. Backscattered Raman radiation was spatially filtered through a 50-μm pinhole (magnified by 10 using a Mitutoyo 20X NA0.4 long-working-length objective lens) to eliminate spurious signal and was collected by custom Raman spectrometers with CCD array detectors (PIXIS 100, Princeton Instruments) equipped with same-turret 300 and 1200/1500 grooves/mm gratings (HR 460, JOBIN YVON for the 488-nm setup and Acton SP2300/2500 of Princeton Instruments for 532 and 660 nm, respectively). The spectral resolution was $\sim$4 cm^{-1}. The diamond Raman edge stress scale [27] was used to determine pressure on decompression with an uncertainty of $\sim$3–5 GPa.

B. Theoretical methods

In this study we relied on the previous structural searches [12], but the use of USPEX yields similar results (not presented here). Structural relaxations and Raman intensity calculations were performed based on the density functional theory (DFT) as implemented in the QUANTUM ESPRESSO code [28]. The norm-conserving pseudopotential [29] was used and the electron-electron exchange and correlation was described by the local-density approximation (LDA) exchange-correlation functional of Ceperley and Alder, as parameterized by Perdew and Zunger (CA-PZ) [30]. The plane-wave cutoff energy was 250 Ry, and a k-point spacing ($2\pi \times 0.03$ Å^{-1}) was used to generate Monkhorst-Pack k-point grids for Brillouin zone sampling [31].

III. RESULTS AND DISCUSSION

A. X-ray diffraction

Room-temperature compression to $P > 40$ GPa results in a diffraction pattern with several low-intensity diffuse peaks. Annealing the samples at 40–102 GPa and 1500–2000 K produces new sharp Bragg reflections that can be indexed with the postaragonite ($Pmmn$) $CaCO_3$ phase [9,18,32]. At 105 GPa, the dominant annealing product is different and forms a new spotty pattern in the XRD images (Fig. 1), but residual broad and diffuse reflections of precursor $CaCO_3$ are also present after the heating. Crystallographic indexing of the new reflections yields monoclinic and orthorhombic solutions with unit cells consistent with the theoretical predictions of $C222_1$ [11] and $P2_1/c$ [12] $CaCO_3$.

Both theoretically proposed models allow indexing the new peaks, yielding almost identical densities at 105 GPa [5.01(2) g/cm^3]. Indeed, topological analysis, performed to reveal structural differences between the two sp^3 $CaCO_3$ structures, shows a high degree of similarity between the $P2_1/c$ and $C222_1$ structures with an identical atomic coordination (Ca$^{[10]}$C$^{[4]}$O$_2^{(5)}$O$^{(4)}$) and arrangement of Ca and C atoms. The only difference between the structures is the orientation of CO_4 tetrahedra: all vertex-sharing helices in $C222_1$ $CaCO_3$ are right-handed, while half helices in the $P2_1/c$ $CaCO_3$ are left-handed (Fig. 2). Despite these similarities, the $P2_1/c$ structure has an approximately 0.2 eV/f.u. lower enthalpy than
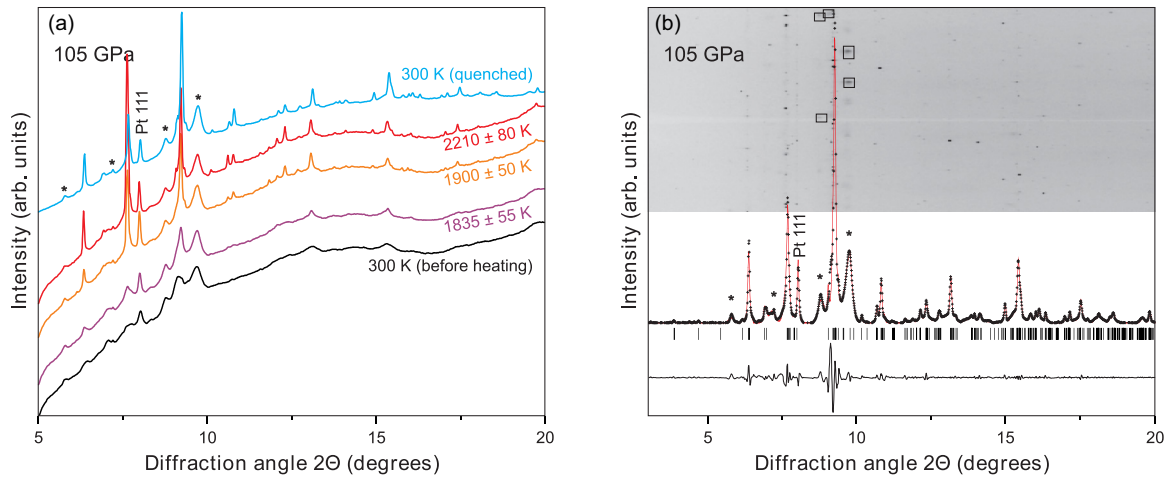
FIG. 1. (a) X-ray diffraction (XRD) of CaCO$_3$ before heating, at T, and after heating at 105 GPa (with background). (b) Le Bail fit of the theoretically predicted $P2_1/c$ CaCO$_3$ (red line) to the experimentally observed XRD pattern (black crosses). The thin black line is the difference curve. The corresponding rectangular diffraction image is shown in the top part. Asterisks and black boxes mark some of the diffuse peaks of remnant CaCO$_3$. X-ray energy is 42 keV.

$C222_1$ CaCO$_3$, according to the computation of Pickard and Needs [12], advocating in favor of the monoclinic structure. Here we provide further support for the $P2_1/c$ CaCO$_3$ as its structural model allows indexing severely split peaks, such as the -112 and 111 Bragg reflections at $\sim 7°$ and the feature at $\sim 9.2°$, 2Θ, as well as other minor reflections in the observed XRD pattern [Fig. 1(b)]. Accordingly, Le Bail refinements of the XRD patterns with the $P2_1/c$ structure systematically yield $\sim 5\%$ better fits than that performed with the $C222_1$ structure. Please note that although we could not perform a full-profile refinement in this work due to the textured XRD pattern, the observed intensities are also consistent with the $P2_1/c$ model [32]. Hence, we confirm the prediction of the $P2_1/c$ CaCO$_3$, albeit at ~ 30 GPa higher than the theoretically predicted sp^2-sp^3 crossover pressure [12]. We note that although $P2_1/c$ and $C222_1$ models of CaCO$_3$ have very similar powder XRD patterns, their Raman spectra may bear significant differences and may help to identify the sp^3 CaCO$_3$ phase.

Depending on the probed sample area, we observed a coexistence of the postaragonite phase with $P2_1/c$ CaCO$_3$ at 103–105 GPa, which indicates that this pressure is close to the phase transition pressure. At 105 GPa and 300 K, the unit-cell parameters of postaragonite CaCO$_3$ are $a = 3.9360(6)$ Å, $b = 4.4372(3)$ Å, and $c = 3.9049(4)$ Å [$\rho = 4.87(2)$ g/cm^3], while those of $P2_1/c$ CaCO$_3$ are $a = 4.5288(13)$ Å, $b = 3.3345(3)$ Å, $c = 9.0927(24)$ Å, and $\beta = 105.57(9)°$ [$\rho = 5.01(2)$ g/cm^3] [32]. The structure of sp^3 CaCO$_3$ is $\sim 3\%$ denser than that of its sp^2-bonded counterpart at 105 GPa (Fig. 3), which is larger than the previously reported density contrasts of 0.5% [19] and 1.25% [9] across the sp^2-sp^3 transition. Importantly, the average carbon-oxygen bond length increases across the phase transition from 1.228 to 1.315 Å (by $\sim 7\%$) as a result of the increased carbon coordination. Note that in order to determine the change in C-O bond length over the sp^2-sp^3 transition in CaCO$_3$ we used the experimentally refined lattice parameters of the coexisting CaCO$_3$ phases at 105 GPa and theoretically computed atomic positions [12].
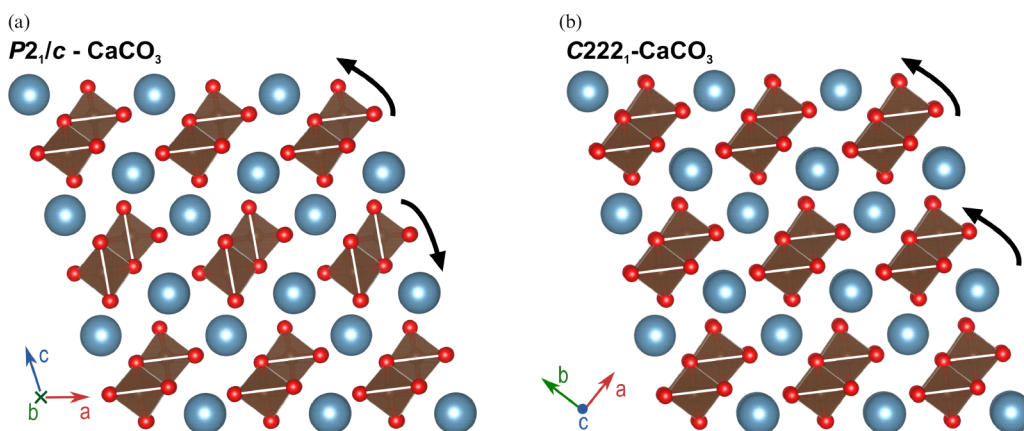

FIG. 2. Structures of (a) $P2_1/c$ CaCO$_3$ and (b) $C222_1$ CaCO$_3$ with outlined CO$_4$ tetrahedra. Calcium atoms are shown in blue, carbon is in brown (inside the polyhedra), and oxygen is in red. Black arrows show the distinct chirality of CO$_4$ tetrahedra chains in the crystal structures.
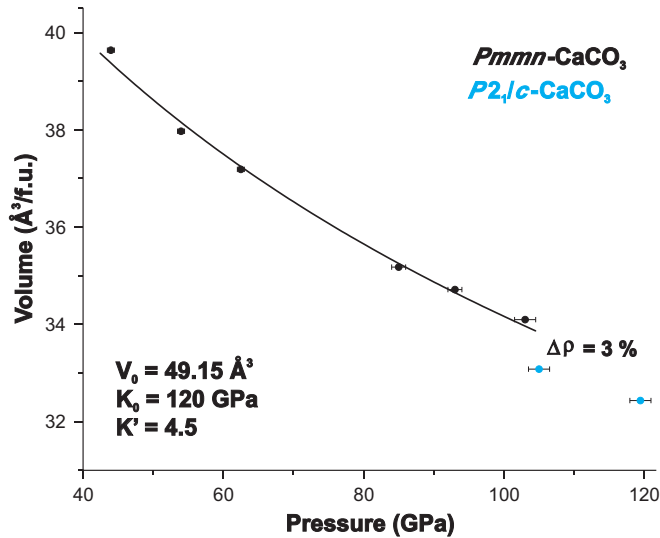
FIG. 3. Pressure-volume relations for *Pmmn* CaCO$_3$ (black dots) and *P*2$_1$/*c* CaCO$_3$ (blue dots). Black line is a 300 K third-order Birch-Murnaghan equation of state (EOS) of *Pmmn* CaCO$_3$ (postaragonite) fitted to the *P-V* data collected here. Best fits were obtained using the previously reported postaragonite V_0 value (49.15 Å^3/f.u.) [18] in combination with K' in the range of 4.5–4.7. Fixing V_0 to the reported value is appropriate because of the larger number of *P-V* measurements in the previous study. Corresponding EOS parameters are given in the bottom left corner. Pressure uncertainty σ is assumed to be 0.5, 1, and 1.5 GPa for $P < 70$, 80–100, and > 100 GPa, respectively.

Although we did not refine the atomic positions based on the experimental XRD, the observed intensities are consistent with the theoretically proposed *P*2$_1$/*c* CaCO$_3$ model [32]. Because of the increase in C-O bond length, one would expect an abrupt decrease in the frequency of the carbon-oxygen stretching vibration across the sp^2-sp^3 transition.

B. Raman spectroscopy

Group theory for *P*2$_1$/*c* CaCO$_3$ allows 30 Raman active vibrations ($15A_g + 15B_g$). Raman spectra collected from the laser-heated area consistently show at least eight new peaks, all of which appear to be characteristic of the vibrational normal modes in the new carbonate as the frequency and relative intensity of these bands are independent of the excitation wavelength (Fig. 4). Particularly important is the new intense band at 1025 cm^{-1}. Considering the increased C-O bond length across the sp^2-sp^3 transition, it is reasonable to suppose that this high-frequency band corresponds to the C-O stretching vibration in the CO$_4$ unit. We have a rough check on this assignment by assuming a harmonic oscillator and an empirically established relation of the force constant and bond length for CX compounds [33]: $f = a(r - 0.61)^{-3}$, where X is a second-period element, a is a constant, and r is the C-X equilibrium bond length. Accepting the change in C-O bond length across the sp^2-sp^3 transition as well as the frequency of C-O symmetric stretching vibration in sp^2 CaCO$_3$ at 105 GPa (1290 cm^{-1}), we obtain a frequency of 1059 cm^{-1} for this vibration in sp^3 CaCO$_3$. This is within 5% of the observed frequency of 1025 cm^{-1}, in support of its assignment to the C-O symmetric stretching in tetrahedral-coordinated carbon. A similar comparison for the graphite-diamond C-C stretch modes yields a frequency of 1273 cm^{-1} for the diamond T_{2g} band at 1 atm, which is again <5% off its actual value (1333 cm^{-1}).

Furthermore, we reproduced the frequencies and intensities of all experimentally observed new Raman bands in our LDA-DFT computations of the Raman spectrum of *P*2$_1$/*c* CaCO$_3$ at 105 GPa [32]. Please note that our computations systematically yielded ~1.5% lower frequencies for all corresponding Raman bands observed in experiment, but when corrected for that, they show remarkable agreement with the experimental spectrum (Fig. 4). Such a correction is justified because LDA-DFT
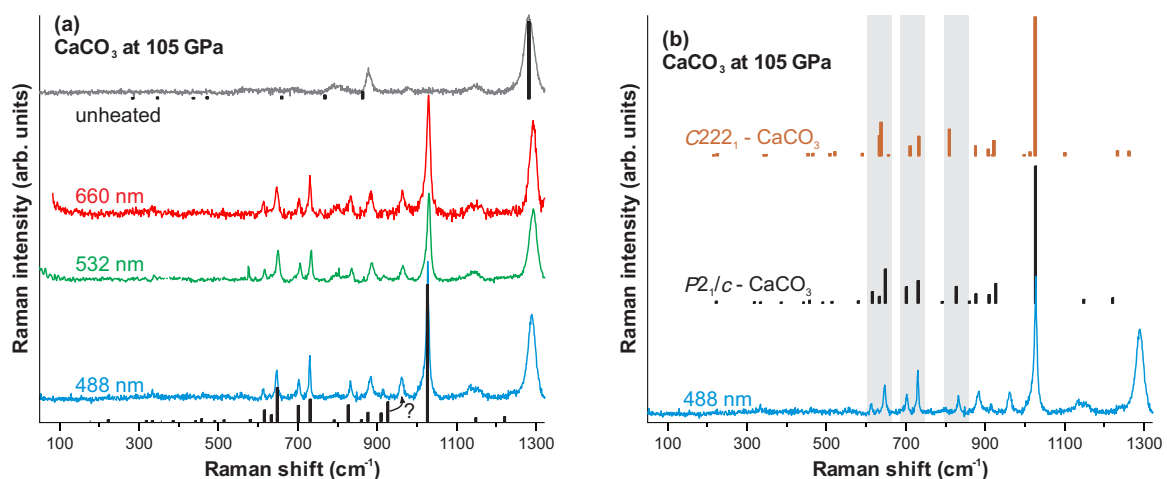

FIG. 4. (a) Raman spectra of CaCO$_3$ at 105 GPa collected with 488-, 532-, and 660-nm excitations. The gray curve is the spectrum of postaragonite CaCO$_3$ collected outside of the heated region. Black vertical bars are computed Raman modes of *P*2$_1$/*c* CaCO$_3$ (bottom) and postaragonite CaCO$_3$ (top) corrected upwards in frequency by 1.5% and 0.5%, respectively. The height of the bars is proportional to the band intensity. The peak indicated by the question mark deviates significantly from the *P*2$_1$/*c* CaCO$_3$ model and may be due to the unheated CaCO$_3$, its yet unidentified phase, or minor nonmolecular CO$_2$ formed upon CaCO$_3$ thermal decomposition on Pt chunks. (b) Experimental spectrum of CaCO$_3$ laser heated at 105 GPa in comparison with the theoretical spectra of *P*2$_1$/*c* and *C*222$_1$ CaCO$_3$ at 105 GPa as computed by LDA-DFT. Gray areas are guides to compare the computed spectra with experiment.
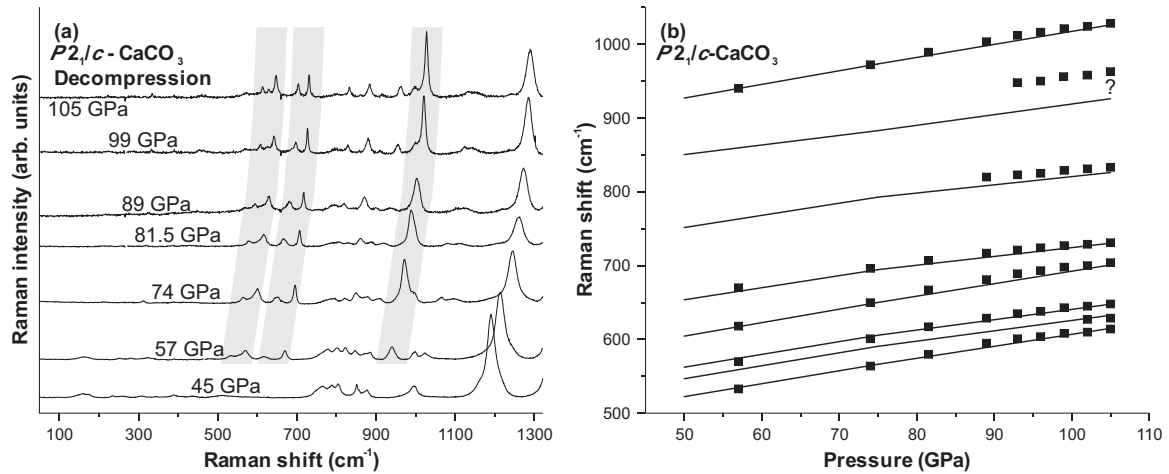
FIG. 5. (a) Raman spectra ($\lambda = 488$ nm) of $CaCO_3$ collected on decompression after laser heating at 105 GPa. Gray areas show characteristic Raman bands of $P2_1/c$ $CaCO_3$. (b) Pressure dependencies of the experimentally observed (squares) and computed (lines) Raman bands of $P2_1/c$ $CaCO_3$ (frequency is corrected upwards by 1.5%). $P2_1/c$ $CaCO_3$ is preserved down to $P = 57$ GPa. The error bar for experimental measurements is not shown as it is smaller than the symbols (black squares).

yields an equilibrium volume that deviates from experimental observations by up to a few percent (e.g., [34]). In addition, we computed a Raman spectrum of $C222_1$ $CaCO_3$ at 105 GPa [32], which, expectedly, shows a C-O vibron frequency (996 cm^{-1}) that is very close to that in $P2_1/c$ $CaCO_3$ (1011 cm^{-1}). Despite this similarity, Raman bands in the 600–850 cm^{-1} spectral range show subtle, yet important, differences between the $C222_1$ and $P2_1/c$ structures. This difference is likely due to the contrasting packing of the CO_4 chains in the structures, which results in slightly different frequencies of deformation modes in CO_4 units. As is clear from Fig. 4(b), the $P2_1/c$ model has better agreement with the experiment than the $C222_1$ structure, providing strong spectroscopic evidence for $P2_1/c$ $CaCO_3$ at 105 GPa.

Upon decompression, we could follow the major Raman bands of sp^3-bonded $CaCO_3$ down to 57 GPa (Fig. 5). The pressure-frequency dependence of these bands appears to be consistent with that computed for $P2_1/c$ $CaCO_3$, in support of the band assignment and product identification. Below 57 GPa, however, we could not observe any Raman bands that can be reliably assigned to $P2_1/c$ $CaCO_3$. Evidently, this indicates a full transformation to an sp^2-bonded $CaCO_3$ phase below 57 GPa, as is also recorded in the intensification of the band at ~1200 cm^{-1}, which is representative of CO_3 groups (symmetric stretch). Identification of this phase was outside the scope of this work. We note, however, that the $CaCO_3$ system is rich in metastable phases (e.g., [16]), and it is possible that the $CaCO_3$ phase formed on unloading to 45 GPa is different from postaragonite.

IV. MECHANISM OF THE sp^2-sp^3 TRANSITION IN CaCO$_3$

To reveal the mechanism of the $Pmmn$ $CaCO_3 \rightarrow$ $P2_1/c$ $CaCO_3$ structural phase transition we performed variable-cell nudged-elastic-band (VCNEB) [35] simulations at 100 GPa, as implemented in the USPEX code [36,37]. First, we obtained an initial trajectory between the two phases using an algorithm developed by Stevanovic *et al.* [38]

(in preparation) to map crystal structures onto each other. The mapping algorithm relies on criteria of minimizing the total Euclidian distance between the corresponding atoms in the end structures and minimizing the change in their coordination along the map (pathway). The initial pathway was subsequently refined by the VCNEB method for the minimum-energy pathway. Both $Pmmn \rightarrow P2_1/c$ and $P2_1/c \rightarrow Pmmn$ paths were prepared (in general, this algorithm may find different paths for forward and backward transitions), and then optimized with VCNEB. The lowest-enthalpy path is presented in detail here. VCNEB calculations required forces and stresses, which were computed by VASP [39] at the Perdew-Burke-Ernzerhof generalized gradient approximation (PBE-GGA) level of theory [40]. Our VCNEB calculations started with 10 intermediate images, and this number automatically increased whenever the path became longer. The climbing image – descending image technique [41] was used to precisely locate transition states (TSs) and intermediate minima [corresponding to potential metastable intermediate phases (IPs)]. Spring constants varied from 3 to 6 eV/Å^2. VCNEB calculations were run for 1000 steps, enabling accurate and well-converging results. At a pressure of 100 GPa, the $P2_1/c$ $CaCO_3$ phase is more stable by 0.02 eV/atom than postaragonite. The barrier height is quite large, 0.14 eV/atom (or 0.70 eV/f.u.), implying that this transition is kinetically feasible only at high temperatures, in agreement with the experimental results of this work.

One important distinction between the crystal structures of sp^2 and sp^3 $CaCO_3$ is that CO_3 groups in postaragonite are isolated, while CO_4 groups in $P2_1/c$ $CaCO_3$ are corner linked into pyroxenelike chains. Accordingly, the transformation mechanism is quite complex and can be divided into four stages (Fig. 6): each stage corresponds to an energy minimum, and boundaries between them correspond to TSs. In the first stage of the transformation, the postaragonite structure distorts gradually, with all CO_3-triangles becoming nonplanar. This distortion becomes critical at transition state 1 (TS$_1$), triggering the second stage of the transition with all carbon atoms forming
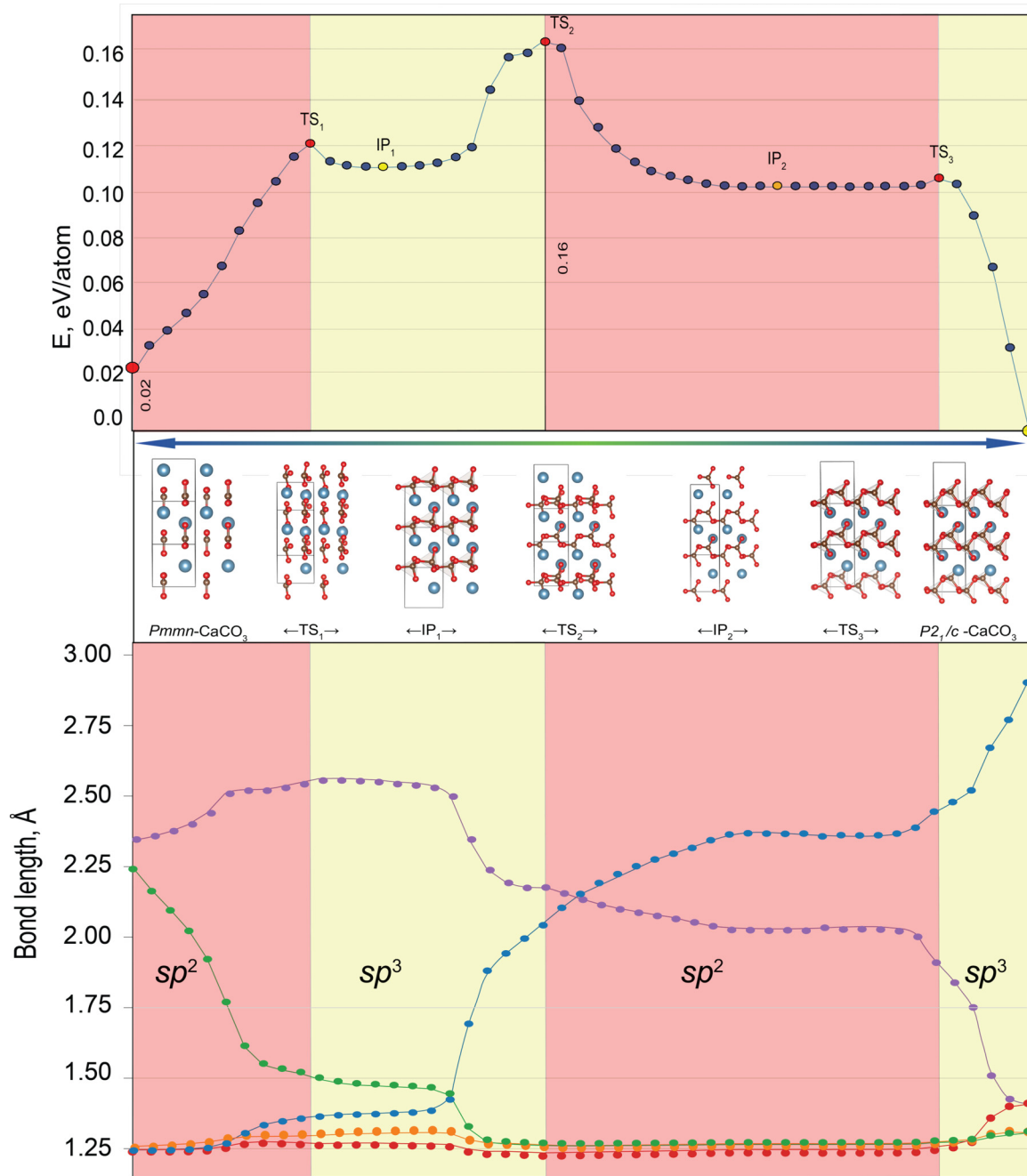
FIG. 6. Mechanism of the Pmmn (postaragonite) $\rightarrow P2_1/c$ transition of CaCO$_3$ at 100 GPa. Structures of initial postaragonite phase; transition states TS$_1$, TS$_2$, and TS$_3$; intermediate phases IP$_1$ and IP$_2$; and final $P2_1/c$ of CaCO$_3$ are shown (for clarity, we highlighted CO$_4$ tetrahedra). The evolution of the five shortest C-O distances is shown across the proposed transition path.

additional bonds with oxygen atoms of the next layer, stitching isolated CO$_3$ groups into infinite chains of CO$_4$ tetrahedra. This topology corresponds to a local enthalpy minimum and has a $P2_1$ symmetry (intermediate phase 1, IP$_1$). However, the enthalpy minimum of IP$_1$ is very shallow (Fig. 6). Towards transition state TS$_2$, one of the C-O bonds of the original CO$_3$ triangle gradually elongates and eventually breaks. In the third stage, between transition states TS$_2$ and TS$_3$, yet another metastable structure with a $P2_1$ symmetry appears, featuring flat and noncoplanar CO$_3$ triangles and a shallow enthalpy minimum. As this structure distorts towards transition state TS$_3$,

carbonate triangles reorient, nearby oxygens displace towards them, and eventually, one obtains infinite chains of CO$_4$ tetrahedra in the same topology as in the $P2_1/c$ structure. The final fourth stage of the transformation is just a relaxation towards the theoretically predicted $P2_1/c$ CaCO$_3$ structure [12].

Transition states define the crossover between different topologies, i.e., the point at which chemical bonds are formed or broken. It is very tempting to think of some maximum bond lengths characteristic of a given pair of atoms (e.g., C-O), beyond which bonds break. However, our results show this not to be the case as the values of

TABLE I. Summary of experimental reports on carbonates with tetrahedrally coordinated carbon.

Reference	System	Space group	P (GPa)	Problems
Ref. [19]	$CaCO_3$	$C222_1$	130	No spectroscopic probe for sp^3 carbon
Ref. [46]	$MgCO_3$	$C2/m$ and $P2_1/a$	82	Le Bail fit; no spectroscopic probe for sp^3 carbon
Ref. [48]	$FeCO_3$		80	Le Bail fit; no spectroscopic probe for sp^3 carbon
Ref. [49]	$(Mg,Fe)CO_3$	$C2/m$ and $P2_1/a$	80	Le Bail fit
Ref. [47]	$(Mg,Fe)CO_3$	$C2/c$	135	No spectroscopic probe for sp^3 carbon

critical C-O bond lengths vary for different transitions. This suggests that the phase transitions are driven not just by the nearest-neighbor interactions but also by longer-range interactions and cooperative effects are important.

Three fundamental comments are necessary regarding the mechanism of this phase transition. First, the intermediate minima (IP_1 and IP_2) in this case are so shallow that they are unlikely to be quenched in the experiment: these minima are not strongly kinetically protected and will rapidly decay into postaragonite and $P2_1/c$, respectively. The role of these intermediate minima is to be "stepping-stones" on the transition pathway, lowering the overall barrier. This is in contrast to the case of BH, a newly predicted compound, where the phase transition involves a very deep and most likely experimentally obtainable, intermediate phase [42]. Second, the transition mechanism discussed here is the best mechanism that we could find (i.e., with the lowest activation enthalpy). However, as we did not perform an exhaustive search over transition paths, we cannot rule out the possibility of other mechanisms. At the moment, there is no algorithm for predicting the globally optimal transition pathway, even within the mean-field picture. Third, the mechanism we just presented is based on the mean-field picture with all unit cells undergoing the same evolution at a given time. In reality, phase transitions occur via nucleation and growth; thus, the mean-field approach accesses crude but crystallographically and intuitively tractable models. Full exploration of nucleation and growth phenomena requires very large systems (with 10^2–10^4 atoms) and advanced sampling techniques, such as transition-path sampling (e.g., [43]); we refer the reader to our recent works employing this methodology (also implemented in the USPEX code) [44,45] and note that such simulations require an accurate force field and, at the *ab initio* level of theory, are computationally unaffordable at the moment.

V. EXPERIMENTAL EVIDENCE FOR sp^3-BONDED CARBONATES

Identification of sp^3-bonded carbonates based solely on XRD is problematic as it requires precise structure determination, which is often challenging at high pressure. Most previous reports on sp^3 carbonates in $MgCO_3$ and $FeCO_3$ systems relied on Le Bail–type fits of theoretically predicted structures to experimentally observed powder-like XRD patterns. For example, Ref. [46] has reported sp^3 $MgCO_3$ at $P \sim 80$ GPa and $T \sim 2000$ K based on the match of XRD to the theoretical prediction of Ref. [11]. One notable exception is the report of $Mg_2Fe_2C_4O_{13}$ with tetrahedrally coordinated carbon at 135 GPa [47] with single-crystal-structure solution methods applied to a multigrain sample synthesized in the $(Mg,Fe)CO_3$

system. We summarize previous experimental reports on sp^3 carbonates in the Table I.

Unlike XRD, vibrational spectroscopy provides bonding fingerprints of the material and is particularly sensitive to the carbon hybridization and chemical environment (e.g., [50]). As such, Raman spectroscopy and/or infrared spectroscopy provide independent evidence for tetrahedrally coordinated carbon and must be used together with crystallographic probes for reliable identification of sp^3 carbonates in high-pressure experiments. Realizing weaknesses of XRD probes in identifying the bond character, Boulard *et al.* [49] reported on synchrotron infrared absorption experiments in $(Mg_{0.25}Fe_{0.75})CO_3$ at 80 GPa, noting a new band that is characteristic of the C-O asymmetric stretching vibration in CO_4 groups. The band assignment relied on first-principles calculations of the infrared spectrum of sp^3 $MgCO_3$ ($P2_1/a$ space group). However, other theoretically predicted bands were not fully assigned in the experiment [49].

In contrast to previous studies, here we provided strong spectroscopic evidence of sp^3 carbonates. Specifically, the intense Raman band at ~ 1025 cm^{-1} (at 105 GPa) and its pressure dependence (~ 1.8 cm^{-1}/GPa) in $P2_1/c$ $CaCO_3$ are characteristic of the symmetrical stretching vibration in its CO_4 groups. In principle, these spectroscopic features can be used in future studies of sp^3 carbonates at high pressure to confirm fourfold carbon coordination.

Our results are also important to validate density functionals used in crystal-structure predictions. Pickard and Needs [12] noted that PBE-GGA and LDA yield essentially similar transition pressures and thus the predicted value is reliable. Here we identified the sp^3 $CaCO_3$ phase and the sp^2-sp^3 crossover pressure (105 GPa), which appears to be ~ 30 GPa higher than the theoretically predicted transition pressure of 76 GPa (at 0 K), suggesting that the entropy term in the free energy is substantial. We showed that high temperature is required to overcome the kinetic barriers associated with the sp^2-sp^3 transition, indicating that complex energy landscapes are typical not only of pure carbon but also of carbonates. As a result, a variety of metastable sp^2 $CaCO_3$ polymorphs have been observed at $P < 40$ GPa [16]. If sp^3-$CaCO_3$ also exhibits rich polymorphism, then the Raman signature of sp^3 carbonates may come in useful for their identification.

VI. GEOCHEMICAL AND GEOPHYSICAL IMPLICATIONS OF sp^3 CARBONATES IN THE LOWERMOST MANTLE

The equilibrium composition of mantle carbonates is governed by the chemical reactions with surrounding minerals [13,14,51] and the thermodynamic stability of corresponding

carbonate phases. Due to the chemical interaction with pyroxene or bridgmanite in the mantle, $CaCO_3$ transforms to Fe-bearing magnesite (up to 10% Fe [52]) at 2–80 GPa [53–56] despite several phase transitions in sp^2 $CaCO_3$ which can modify the chemical equilibrium in this pressure range [9,12]. Also, the spin transition in Fe-bearing $MgCO_3$ at $P \sim 45$ GPa may promote iron solubility in the carbonate phase due to crystal-field effects [57] and the ionic size similarity of low-spin Fe^{2+} to Mg^{2+} [58], but this has never been quantitatively addressed in experiment. The sp^2-sp^3 transition in $MgCO_3$ at $P \sim 80$ GPa further upholds the Mg-rich carbonate composition, as revealed by a computation of enthalpies in the reaction $MgCO_3 + CaSiO_3 = CaCO_3 + MgSiO_3$ as a function of pressure and accounting for phase transitions [11,12]. The theoretically predicted sp^2-sp^3 transition in $CaCO_3$ at 76 GPa eventually stabilizes $CaCO_3$ against $MgCO_3$ at $P >$ ~ 100 GPa [12]. Here we have synthesized the predicted $P2_1/c$ $CaCO_3$ at $P \sim 105$ GPa and $T \sim 2000$ K, about 30 GPa higher than the theoretically predicted sp^2-sp^3 transition pressure at 0 K. Taking into account this 30 GPa difference, we propose that the crossover to Ca carbonates in Earth (i.e., at high temperature) may be expected at $P \sim 135$ GPa, which corresponds to the pressure at the core-mantle boundary. This inference can be tested via high-pressure studies of chemical reactions in mechanical mixtures of $MgCO_3$ with $CaSiO_3$ or $CaCO_3$ with $MgSiO_3$ at high pressure and temperature.

VII. CONCLUSIONS

In summary, we located the sp^2-sp^3 transition in $CaCO_3$ and identified the $P2_1/c$ $CaCO_3$ at $P > 105$ GPa using x-ray diffraction and Raman spectroscopy. Using first-principles methods, we showed that the mechanism of the sp^2-sp^3 crossover in $CaCO_3$ involves several intermediate phases with sp^2 and sp^3 bonding motifs. Finally, our results support the idea of the crossover in the carbonate crystal chemistry that leads to Ca-rich carbonates at the base of the mantle.

[1] F. P. Bundy, W. A. Bassett, M. S. Weathers, R. J. Hemley, H. K. Mao, and A. F. Goncharov, Carbon **34**, 141 (1996).

[2] J. E. Field, *The Properties of Natural and Synthetic Diamond* (Academic, London, 1992).

[3] V. D. Blank, S. G. Buga, G. A. Dubitsky, N. R. Serebryanaya, M. Y. Popov, and B. Sundqvist, Carbon **36**, 319 (1998).

[4] Y. Lin, L. Zhang, H. K. Mao, P. Chow, Y. M. Xiao, M. Baldini, J. F. Shu, and W. L. Mao, Phys. Rev. Lett. **107**, 175504 (2011).

[5] R. C. Powles, N. A. Marks, D. W. M. Lau, D. G. McCulloch, and D. R. McKenzie, Carbon **63**, 416 (2013).

[6] A. A. Godovikov, *Mineralogiia* (Nedra, Moscow, 1975).

[7] F. Liebau, *Structural Chemistry of Silicates: Structure, Bonding, and Classification* (Springer, Berlin, 1985).

[8] N. V. Skorodumova, A. B. Belonoshko, L. Huang, R. Ahuja, and B. Johansson, Am. Mineral. **90**, 1008 (2005).

[9] A. R. Oganov, C. W. Glass, and S. Ono, Earth Planet. Sci. Lett. **241**, 95 (2006).

[10] S. Arapan, J. S. De Almeida, and R. Ahuja, Phys. Rev. Lett. **98**, 268501 (2007).

[11] A. R. Oganov, S. Ono, Y. M. Ma, C. W. Glass, and A. Garcia, Earth Planet. Sci. Lett. **273**, 38 (2008).

[12] C. J. Pickard and R. J. Needs, Phys. Rev. B **91**, 104101 (2015).

[13] I. Martinez, J. Z. Zhang, and R. J. Reeder, Am. Mineral. **81**, 611 (1996).

[14] K. Sato and T. Katsura, Earth Planet. Sci. Lett. **184**, 529 (2001).

[15] K. Catalli and Q. Williams, Am. Mineral. **90**, 1679 (2005).

[16] M. Merlini, M. Hanfland, and W. A. Crichton, Earth Planet. Sci. Lett. **333-334**, 265 (2012).

[17] T. Pippinger, R. Miletich, M. Merlini, P. Lotti, P. Schouwink, T. Yagi, W. A. Crichton, and M. Hanfland, Phys. Chem. Miner. **42**, 29 (2015).

[18] S. Ono, T. Kikegawa, Y. Ohishi, and J. Tsuchiya, Am. Mineral. **90**, 667 (2005).

[19] S. Ono, T. Kikegawa, and Y. Ohishi, Am. Mineral. **92**, 1246 (2007).

[20] N. C. Holmes, J. A. Moriarty, G. R. Gathers, and W. J. Nellis, J. Appl. Phys. **66**, 2962 (1989).

[21] V. B. Prakapenka, A. Kubo, A. Kuznetsov, A. Laskin, O. Shkurikhin, P. Dera, M. L. Rivers, and S. R. Sutton, High Pressure Res. **28**, 225 (2008).

[22] C. Prescher and V. Prakapenka, High Pressure Res. **35**, 223 (2015).

[23] B. H. Toby, J. Appl. Crystallogr. **34**, 210 (2001).

[24] A. C. Larson and R. B. Von Dreele, General Structure Analysis System (GSAS), Los Alamos National Laboratory Report LAUR 86-748 (2004).

[25] J. Gonzalez-Platas, M. Alvaro, F. Nestola, and R. Angel, J. Appl. Crystallogr. **49**, 1377 (2016).

[26] K. Momma and F. Izumi, J. Appl. Crystallogr. **44**, 1272 (2011).

[27] Y. Akahama and H. Kawamura, J. Appl. Phys. **100**, 043516 (2006).

[28] P. Giannozzi *et al.*, J. Phys.: Condens. Matter **21**, 395502 (2009).

[29] D. R. Hamann, M. Schluter, and C. Chiang, Phys. Rev. Lett. **43**, 1494 (1979).

[30] D. M. Ceperley and B. J. Alder, Phys. Rev. Lett. **45**, 566 (1980).

[31] H. J. Monkhorst and J. D. Pack, Phys. Rev. B **13**, 5188 (1976).

[32] See Supplemental Material at http://link.aps.org/supplemental/10.1103/PhysRevB.96.104101 for additional synchrotron x-ray diffraction pattern and tabulated vibrational properties of $CaCO_3$ polymorphs.

[33] E. Kurita, H. Matsuura, and K. Ohno, Spectrochim. Acta A **60**, 3013 (2004).

[34] H. Hsu, K. Umemoto, M. Cococcioni, and R. M. Wentzcovitch, Phys. Earth Planet. Inter. **185**, 13 (2011).

[35] G. R. Qian, X. Dong, X. F. Zhou, Y. J. Tian, A. R. Oganov, and H. T. Wang, Comput. Phys. Commun. **184**, 2111 (2013).

[36] A. R. Oganov and C. W. Glass, J. Chem. Phys. **124**, 244704 (2006).

[37] A. O. Lyakhov, A. R. Oganov, H. T. Stokes, and Q. Zhu, Comput. Phys. Commun. **184**, 1172 (2013).

[38] V. Stevanovic, R. Trottier, F. Therrien, C. Musgrave, A. Holder, and P. Graf (unpublished).

[39] G. Kresse and J. Furthmuller, Phys. Rev. B **54**, 11169 (1996).

[40] J. P. Perdew, K. Burke, and M. Ernzerhof, Phys. Rev. Lett. **77**, 3865 (1996).

[41] G. Henkelman, B. P. Uberuaga, and H. Jonsson, J. Chem. Phys. **113**, 9901 (2000).

[42] C. H. Hu, A. R. Oganov, Q. Zhu, G. R. Qian, G. Frapper, A. O. Lyakhov, and H. Y. Zhou, Phys. Rev. Lett. **110**, 165504 (2013).

[43] P. G. Bolhuis, D. Chandler, C. Dellago, and P. L. Geissler, Annu. Rev. Phys. Chem. **53**, 291 (2002).

[44] S. E. Boulfelfel, A. R. Oganov, and S. Leoni, Sci. Rep. **2**, 471 (2012).

[45] B. X. Li, G. R. Qian, A. R. Oganov, S. E. Boulfelfel, and R. Faller, J. Chem. Phys. **146**, 214502 (2017).

[46] E. Boulard, A. Gloter, A. Corgne, D. Antonangeli, A. L. Auzende, J. P. Perrillat, F. Guyot, and G. Fiquet, Proc. Natl. Acad. Sci. U.S.A. **108**, 5184 (2011).

[47] M. Merlini, M. Hanfland, A. Salamat, S. Petitgirard, and H. Muller, Am. Mineral. **100**, 2001 (2015).

[48] E. Boulard *et al.*, J. Geophys. Res. **117**, B02208 (2012).

[49] E. Boulard, D. Pan, G. Galli, Z. X. Liu, and W. L. Mao, Nat. Commun. **6**, 6311 (2015).

[50] E. Stavrou, S. Lobanov, H. F. Dong, A. R. Oganov, V. B. Prakapenka, Z. Konopkova, and A. F. Goncharov, Chem. Mater. **28**, 6925 (2016).

[51] J. A. Dalton and B. J. Wood, Earth Planet. Sci. Lett. **119**, 511 (1993).

[52] V. Stagno, Y. Tange, N. Miyajima, C. A. McCammon, T. Irifune, and D. J. Frost, Geophys. Res. Lett. **38**, L19309 (2011).

[53] I. Kushiro, H. Satake, and S. Akimoto, Earth Planet. Sci. Lett. **28**, 116 (1975).

[54] G. Brey, W. R. Brice, D. J. Ellis, D. H. Green, K. L. Harris, and I. D. Ryabchikov, Earth Planet. Sci. Lett. **62**, 63 (1983).

[55] C. Biellmann, P. Gillet, F. Guyot, J. Peyronneau, and B. Reynard, Earth Planet. Sci. Lett. **118**, 31 (1993).

[56] Y. Seto, D. Hamane, T. Nagai, and K. Fujino, Phys. Chem. Miner. **35**, 223 (2008).

[57] S. S. Lobanov, A. F. Goncharov, and K. D. Litasov, Am. Mineral. **100**, 1059 (2015).

[58] B. Lavina, P. Dera, R. T. Downs, V. Prakapenka, M. Rivers, S. Sutton, and M. Nicol, Geophys. Res. Lett. **36**, L23306 (2009).